

Research Article

Single-Atom Ni Heterogeneous Catalysts Supported UiO-66 Structure: Synthesis and Catalytic Activities

Le Thi Hoa,¹ Le Thi Thanh Nhi,^{1,2} Le Van Thanh Son,³ Nguyen Le My Linh,⁴
Ho Van Minh Hai ¹ and Dinh Quang Khieu ¹

¹University of Sciences, Hue University, 49000, Vietnam

²Duy Tan University, 50000, Vietnam

³University of Education and Science, The University of Da Nang, 50000, Vietnam

⁴University of Education, Hue University, 49000, Vietnam

Correspondence should be addressed to Ho Van Minh Hai; hvmhai@hueuni.edu.vn
and Dinh Quang Khieu; dqkhieu@hueuni.edu.vn

Received 16 December 2020; Revised 20 January 2021; Accepted 20 April 2021; Published 19 May 2021

Academic Editor: Ovidiu Ersen

Copyright © 2021 Le Thi Hoa et al. This is an open access article distributed under the Creative Commons Attribution License, which permits unrestricted use, distribution, and reproduction in any medium, provided the original work is properly cited.

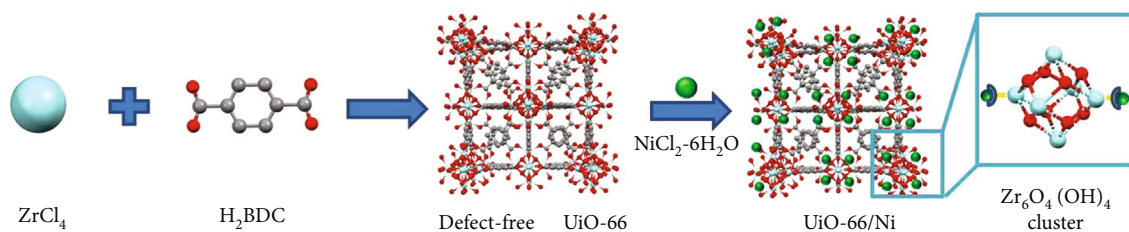
Herein, the single-atom Ni site heterogeneous catalysts supported by the UiO-66 structure (University of Oslo-66 metal organic framework) were successfully synthesized by a postsynthetic metalation method, where Ni ions are covalently attached to the missing-linker defect sites at zirconium oxide clusters ($Zr_6O_4(OH)_4$) in as-prepared UiO-66 structure, $[Zr_6O_4(OH)_4(BDC)(DMF)_{10}(OH)_{10}]$ (BDC (benzene-1,4-dicarboxylate), DMF (dimethylformamide)). The structure properties of the catalysts were characterized using powder X-ray diffraction (PXRD), Fourier transform infrared (FT-IR), scanning electron microscopy (SEM), transmission electron microscopy (TEM), energy-dispersive X-ray spectroscopy (EDX), N_2 adsorption-desorption isotherms (BET), thermogravimetric analysis (TGA), X-ray photoelectron spectroscopy (XPS), and photoluminescence spectroscopy (PL). It was found that single-atom Ni heterogeneous catalysts supported by the UiO-66 structure, UiO-66/Ni1.0 $[Zr_6O_4(OH)_4(C_8H_4O_4)(DMF)_{10}(OH)_8Ni_2(OH)_2(Cl)_2]$, showed a sphere-like morphology with a high specific surface area as well as good thermal stability. Specifically, the as-prepared UiO-66/Ni1.0 exhibited the excellent catalytic activity and stability for 4-nitrophenol reduction in terms of low activation energy ($E_a = 23.15 \text{ kJ mol}^{-1}$), high turnover frequency ($76.19 \text{ molecules g}^{-1} \text{ min}^{-1}$), and high apparent rate constant ($k_{app} = 0.956 \text{ min}^{-1}$). In addition, methylene blue (MB) was also chosen as the organic dye model for catalytic reduction reaction. The k_{app} and TOF for the reduction of MB using UiO-66/Ni1.0 were 0.787 min^{-1} and $33.89 \times 10^{20} \text{ molecules g}^{-1} \text{ min}^{-1}$, respectively.

1. Introduction

Nitroaromatic compounds, especially 4-nitrophenol (4-NP), are extensively employed in the fields of pigments, pharmaceuticals, dyes, explosives, plastics, pesticides, wood, or leather preservative [1–7]. However, 4-nitrophenol (4-NP), known as the toxic and highly hazardous contaminants, is found in agricultural and industrial wastewaters [8–10]. This compound released from above industrial sectors can impact negatively on the ecological system and pose serious environmental pollution. It is worth noting that the exposure of 4-NP would threaten human health such as damage to the

nervous central system, blood system, and primary organs [11–13]. In addition to this, methylene blue (MB), known as organic dye, is broadly studied because of its many potential applications in industries such as printing, textile, paper, paints, and plastics [14]. It is noticeable that methylene blue is also a high-toxicity carcinogenic organic compound and can be a cause of water environmental pollution [15, 16].

Due to this reason, it is necessary to develop the simple, efficient method for removal of these organic compounds in wastewaters. Recently, many various technologies such as adsorption, photocatalytic degradation, chemical oxidation, and membrane filtration have been applied to remove these



SCHEME 1: The scheme of the formation process of the UiO-66/Ni catalyst. Atom label: C: grey; O: red; Zr: sky blue; Ni: green (H atoms are omitted for clarity).

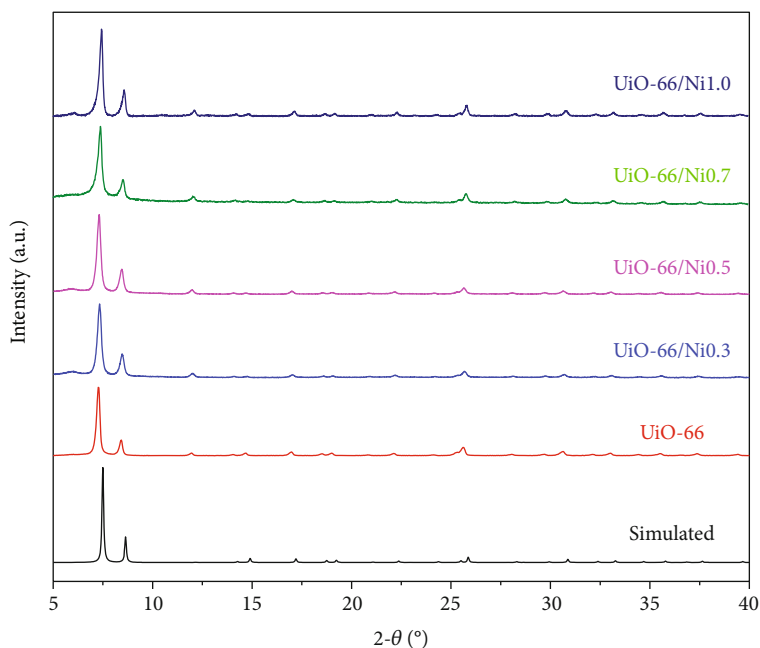


FIGURE 1: PXRD patterns of UiO-66 and UiO-66/Nix ($x = 0.3, 0.5, 0.7, \text{ and } 1.0$).

compounds with the aim of reducing the risks [17–20]. In particular, the catalytic reduction can be considered as an effective and facile route to remove these organic pollutants [21–24]. Thus, many efforts have been devoted to the design of the suitable catalyst structure, which can significantly improve the reduction efficiency, providing excellent catalytic sustainability and recoverability.

Metal oxides, metal nanoparticles, and metal complexes can be employed as promising candidates in a wide range of heterogeneous catalytic fields [25–27]. The active metal sites are normally located at crystal corners, edges, and facets which exhibit the diverse catalytic properties [28]. Among these above-mentioned heterogeneous metal catalysts, metal complexes are known as single-site heterogeneous catalysts which have attracted increasing attention in recent years [29–32]. These exposed identical site-isolated metal centers can easily bond and react with reactant molecules in solution. In order to synthesize single-site heterogeneous catalysts, one of the simplest methods is to anchor catalytically active metal atoms, cations, or complexes directly to high surface area solid supports.

Metal-organic frameworks (MOFs) are known as porous material, and the crystalline structure consists of a metal clus-

ter connected by organic linker molecules [33–36]. The abundance of MOFs' structure was derived from the diverse combination of metal clusters and organic components which has been intensively investigated for a wide range of application such as gas adsorption, catalysis, energy storage, sensing, and drug delivery [37–40]. Recently, many works have demonstrated that the existence of missing-linker defects on MOFs has significantly influenced the material properties [41–43]. In this case, an outstanding example is UiO-66 which has attracted considerable attention due to its chemical, mechanical, and thermal stability [44]. The crystal structure of UiO-66 consists of zirconium oxide clusters ($\text{Zr}_6\text{O}_4(\text{OH})_4$) connected to six benzene-1,4-dicarboxylate (H_2BDC) linkers, leading to the formation of the 3D framework. However, the UiO-66 structure has been identified to contain defect sites at zirconium oxide clusters, where a linker is missed such as water and hydroxide [45–47]. By utilizing the postsynthetic metalation method, the UiO-66 structure with a high surface provides a highly tunable platform to design single-site heterogeneous catalysts.

In this study, we report a simple route to synthesize the single-site heterogeneous catalyst UiO-66/Ni, where Ni atoms are to anchor to the missing-linker defect sites at

TABLE 1: Elemental composition of as-prepared UiO-66 and UiO-66/Ni analyzed by EDX.

Samples	C	O	Zr	Atom (%)		Ni/Zr ratio	Ni/Cl ratio
				Ni	Cl		
UiO-66	60.96	35.91	3.12	—	—	—	—
UiO-66/Ni0.3	51.27	44.49	3.77	0.18	0.3	0.048	1.333
UiO-66/Ni0.5	50.03	46.58	3.03	0.2	0.16	0.066	1.250
UiO-66/Ni0.7	55.91	40.85	2.79	0.23	0.22	0.082	1.045
UiO-66/Ni1.0	54.59	42.14	2.78	0.24	0.24	0.086	1.000

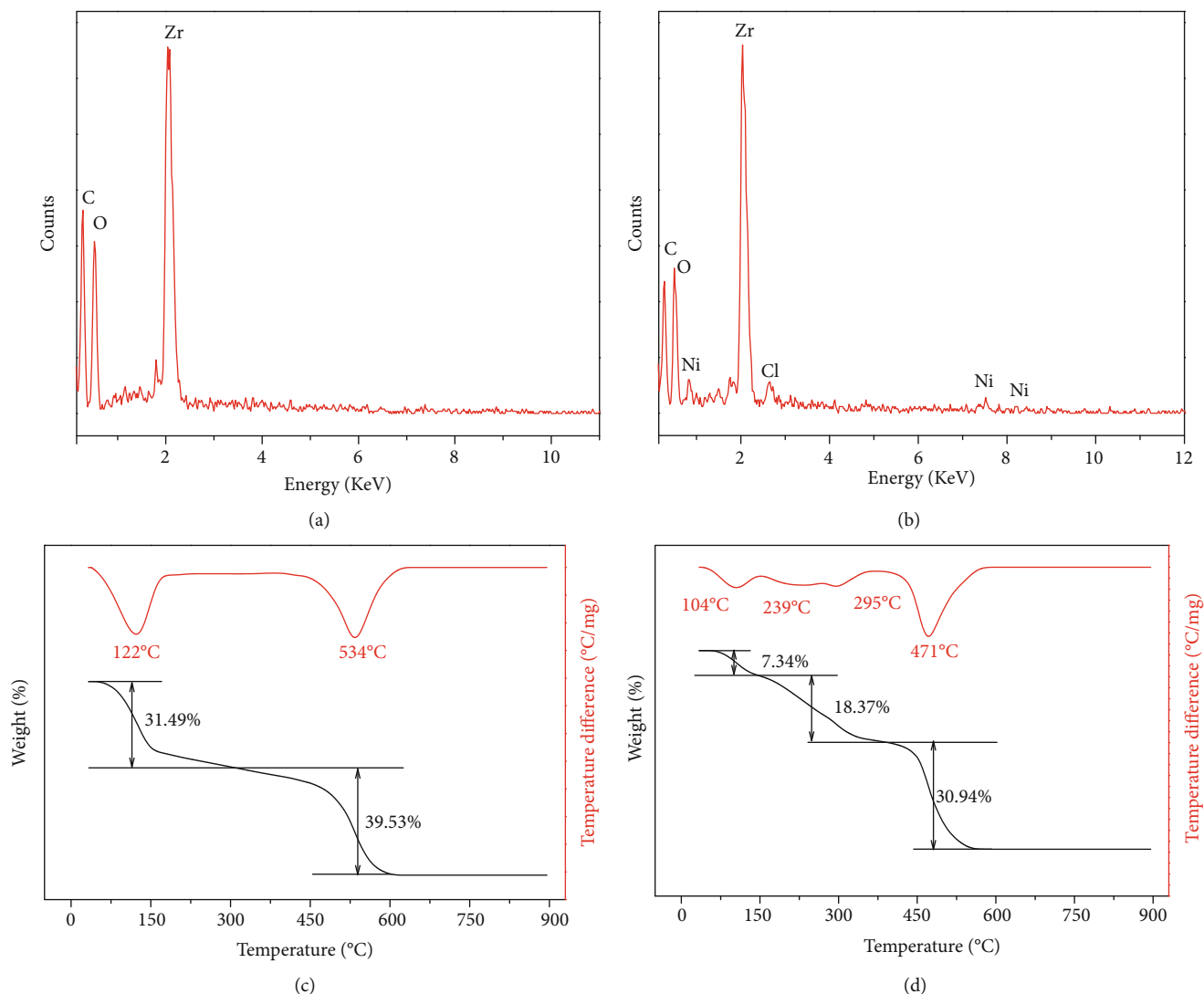


FIGURE 2: Energy-dispersive X-ray (EDX) spectra and the TG-DTA diagrams of UiO-66 (a, c) and UiO-66/Ni1.0 (b, d).

zirconium oxide clusters ($Zr_6O_4(OH)_4$) in the as-prepared UiO-66 structure, $Zr_6O_4(OH)_4(C_8H_4O_4)(DMF)_{10}(OH)_{10}$. By this strategy, active Ni sites can be inherently located at the pore surfaces with the host as-prepared UiO-66 frameworks well retained, which will significantly enhance the free diffusion of reactant molecules. Thus, single-atom Ni site heterogeneous catalysts exhibit the highly efficient reduction catalysis toward 4-nitrophenol and methylene blue.

2. Experiment

2.1. Materials. Zirconium tetrachloride ($ZrCl_4$, 99%), 1,4-benzenedicarboxylic acid (H_2BDC , 97%), N,N' -dimethylformamide (DMF, 99%), nickel(II) chloride hexahydrate ($NiCl_2 \cdot 6H_2O$, 97.0%) methanol (CH_3OH , 99%), and 4-nitrophenol ($C_6H_5NO_3$, 99%) were used without further purification and purchased from the Merck Company, Germany.

2.2. Instrumental Characterization. Powder X-ray diffraction (PXRD) analysis was carried out on a D8 Advanced Bruker anode X-ray diffractometer with $\text{CuK}\alpha$ ($\lambda = 1.5406 \text{ \AA}$) radiation. The morphology of the samples was observed by scanning electron microscopy (Hitachi S-4800). The transmission electron microscopy (TEM) images were obtained using a JEOL JEM-2100 transmission electron microscope at 200 kV. Fourier transformation infrared analyses were recorded on a Shimadzu IRPrestige-21 (Japan). Nitrogen adsorption/desorption isotherms were measured using a Micromeriti CMS 2020 volumetric adsorption analyzer system. The samples were degassed by heating under vacuum at 393 K for 24 h. The specific surface area of the samples was calculated using the Brunauer–Emmett–Teller (BET) model. X-ray photoelectron spectroscopy (XPS) was recorded with a Kratos Analytical spectrometer. All binding energies were referenced to the contaminant C 1s peak (at 284.6 eV) of adventitious carbon. Thermogravimetric analysis (TGA) was carried out using a TG-DTA instrument (DTG-60H Shimadzu) under atmospheric pressure at a heating rate of $10^\circ\text{C min}^{-1}$. Photoluminescence spectroscopy (PL) was measured at room temperature with a photoluminescence spectrophotometer (Horiba FL3). The concentration of 4-nitrophenolate was measured using a UV-vis spectrophotometer (V-630 Jasco) at λ_{max} 400 nm.

2.3. Synthesis of Materials

2.3.1. Synthesis of UiO-66. In a typical process, ZrCl_4 (0.53 g, 2.274 mmol) and H_2BDC (0.38 g, 2.287 mmol) were dissolved into $\text{N,N}'$ -dimethylformamide (60 mL) to form homogeneous solution at room temperature. Next, the obtained solution was transferred into a Teflon-lined autoclave and maintained at 120°C for 36 h. The white solids were then collected and washed with $\text{N,N}'$ -dimethylformamide and methanol, respectively. Finally, the resulting products were dried at 60°C for 24 h in the oven to obtain UiO-66.

2.3.2. Synthesis of UiO-66/Ni. UiO-66/Ni was synthesized by a postsynthetic metalation method [48]. As-prepared UiO-66 (0.1 g) was transferred into a glass vial, which contained 10 mL of $\text{N,N}'$ -dimethylformamide. After sonication for 1 min, a certain amount of $\text{NiCl}_2 \cdot 6\text{H}_2\text{O}$ (0.3, 0.5, 0.7, and 1.0 mmol) was added into the suspension solution. Then, the vial was sealed, heated, and maintained at 90°C for 24 h. The slight blue solids were collected and washed with $\text{N,N}'$ -dimethylformamide and methanol, respectively. The final products of UiO-66/Ni were finally dried at 60°C for 24 h in the oven and named UiO-66/Nix (x : 0.3, 0.5, 0.7, and 1.0).

2.4. Catalytic Activity of UiO-66/Ni. The reduction reaction of 4-nitrophenol with the presence of NaBH_4 solution was used to evaluate the catalytic activity of the UiO-66/Ni catalyst. In this study, the reaction process was performed in a quartz cuvette, and UV-vis spectroscopy was intermittently recorded at room temperature. Initially, 3.0 mL of aqueous 4-NP solution 20 mg L^{-1} and 5.0 mg of NaBH_4 were alternately transferred into a quartz cuvette. The obtained solu-

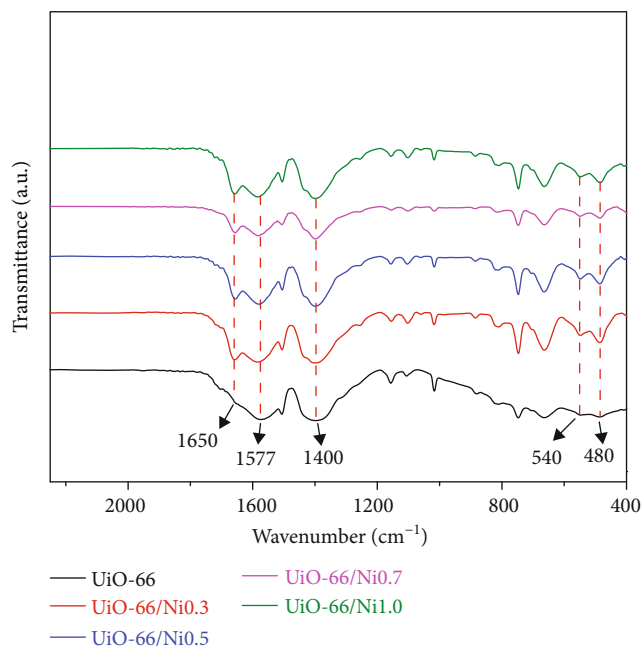


FIGURE 3: The Fourier transform infrared spectra (FTIR) of as-prepared UiO-66 and UiO-66/Nix.

tion mixture color changed immediately to deep yellow. Then, 5.0 mg of UiO-66/Ni was dispersed in 1.0 mL of deionized water with the assistance of sonication for 1 hour to yield a stable suspension. Subsequently, $5 \mu\text{L}$ of the obtained UiO-66/Ni dispersion liquid (5 mg mL^{-1}) was dropped into the above yellow solution. UV-vis absorption spectroscopy was recorded to determine the reaction progress. 4-NP conversion was calculated as the following equation:

$$\text{Conversion}(\%) = \frac{C_0 - C_t}{C_0} \times 100\%, \quad (1)$$

where C_0 is the initial concentration of 4-NP and C_t is the concentration of 4-NP at time t . The catalytic reduction of methylene blue (MB) by NaBH_4 with the presence of the UiO-66/Ni catalyst was also investigated similarly to the procedure for the catalytic reduction of 4-NP.

3. Results and Discussion

3.1. Characterization of Materials. Scheme 1 illustrates the schematic diagram of the formation process of UiO-66/Ni. Firstly, UiO-66 is synthesized by a one-step solvothermal method. Then, nickel single atoms are introduced onto the UiO-66 framework through a postsynthetic metalation method. The crystal structure description of as-synthesized UiO-66 is shown in Scheme 1. As can be seen, the UiO-66 exhibits face-centered-cubic crystal structure, and the structure symmetry was identified as the $\text{Fm}\bar{3}\text{m}$ space group. Each zirconium metal is coordinated to 8 oxygen atoms which belong to four H_2BDC linkers, and six of them connect together, leading to the formation of the $\text{Zr}_6\text{O}_4(\text{OH})_4$ metal center. It is noticeable that each $\text{Zr}_6\text{O}_4(\text{OH})_4$ metal center is connected to six H_2BDC linkers to create the 3D framework

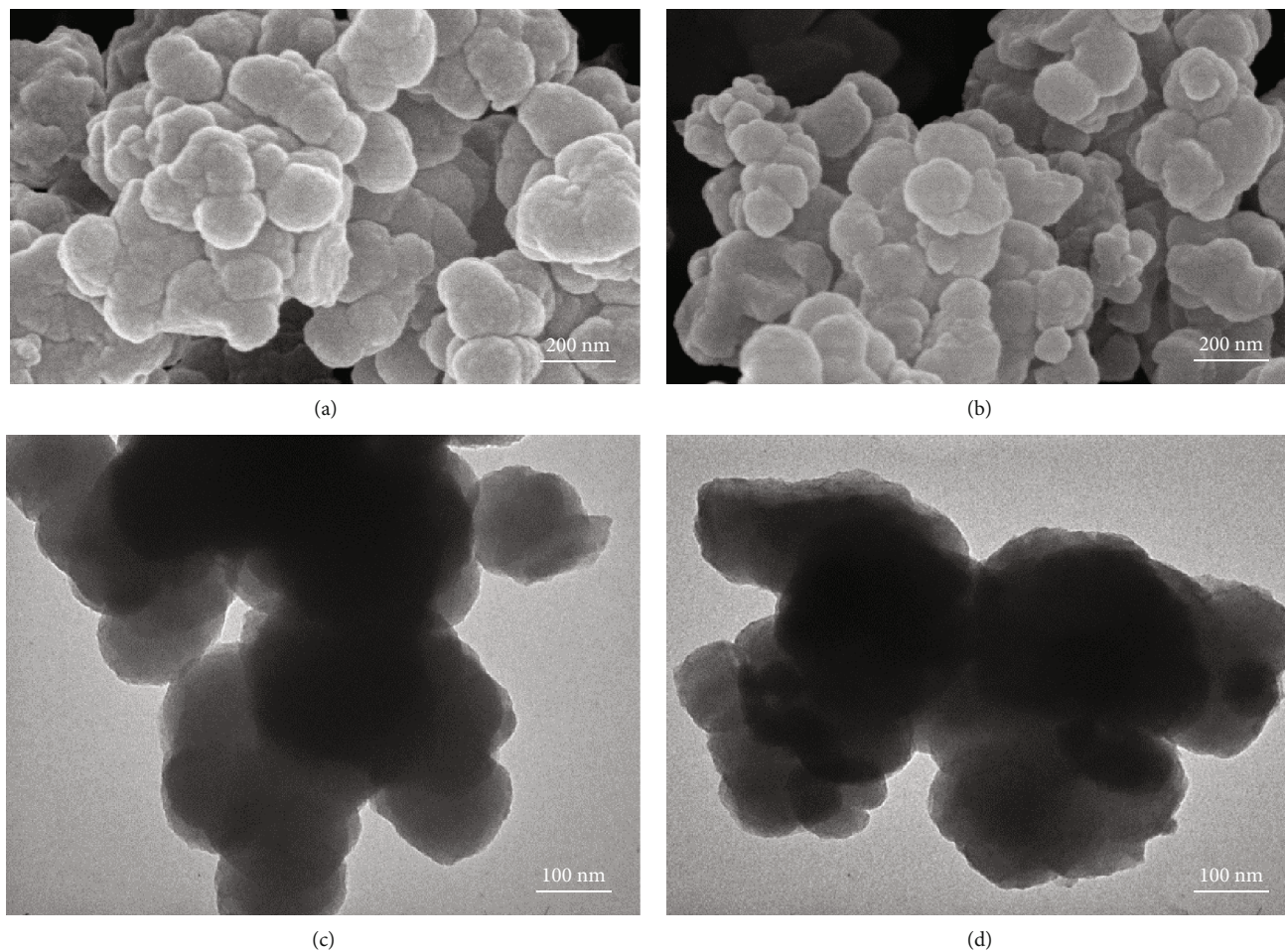
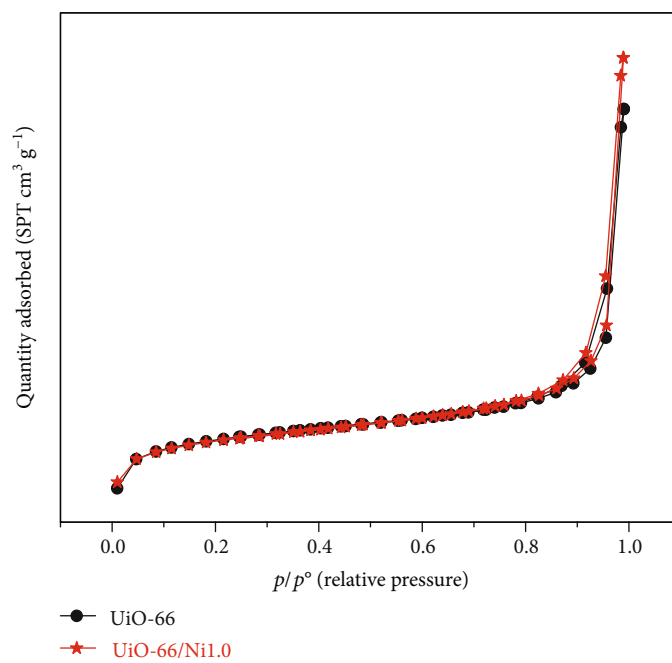


FIGURE 4: SEM and TEM images of UiO-66 (a, c) and UiO-66/Ni1.0 (b, d).

FIGURE 5: N_2 adsorption-desorption isotherms of as-prepared UiO-66 and UiO-66/Ni1.0.

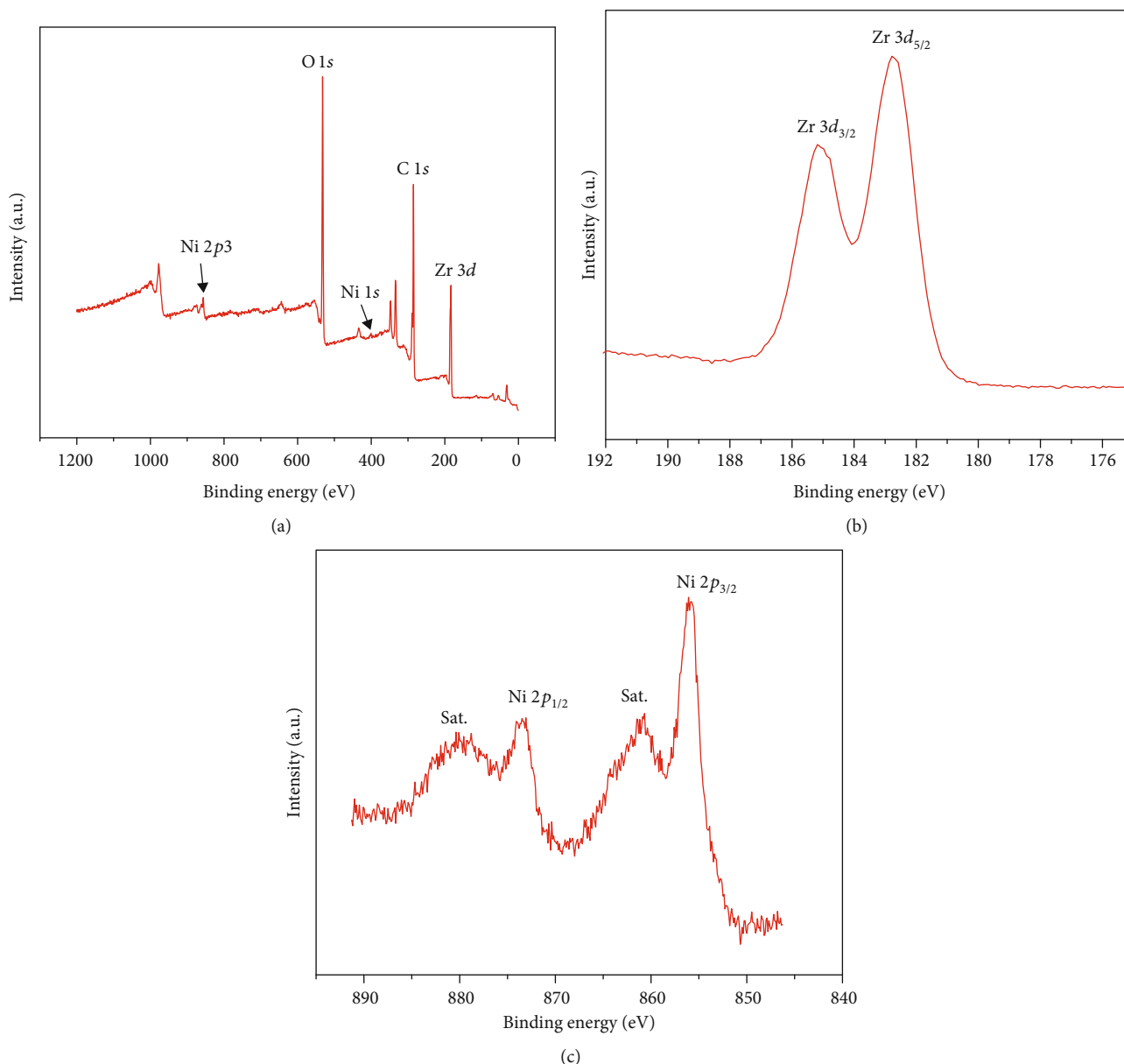


FIGURE 6: XPS survey scan of UiO-66/Ni1.0 (a) and core scan spectra of (b, c) C1s, O1s, Ni 2p, and Zr 3d.

with the high degree of network connection. This can be explained for its high stability in most chemical solvent and stable up to 500°C in air atmosphere [49]. It is worth noting that the UiO-66 structure demonstrated the existence of linker vacancies which are located in terminate -OH/OH₂ groups of the Zr₆O₄(OH)₄ metal center. The amount of defect sites depends on the synthetic protocol. In this study, the stoichiometric formula of the as-prepared UiO-66 was hypothesized as follows: Zr₆O₄(OH)₄(C₈H₄O₄)_x(DMF)_{12-2x}(OH)_{12-2x}. Hydroxide groups and DMF can be used for charge balancing and completing the coordination clusters of the Zr₆O₄(OH)₄ metal center. Then, as-prepared UiO-66 was immersed in solution of NiCl₂·6H₂O in DMF at 90°C for 24 h with the aim of anchoring Ni atoms at the oxygen atoms of -OH/OH₂ groups, leading to the formation of the UiO-66/Ni structure.

The structure and crystal phase of the as-prepared UiO-66 and UiO-66/Ni with different concentrations of the nickel precursor were determined by the PXRD analysis, as shown in Figure 1. It is clearly seen that all of the diffraction peaks of UiO-66 and UiO-66/Ni were well matched with the simulated PXRD pattern of hydroxylated UiO-66, indicating that the as-prepared UiO-66 was successfully synthesized with a high degree of crystallinity. It is noticeable that the characteristic diffraction peaks of NiO and other nickel atom contained compound nanoparticles not observed in Figure 1. This result can be explained to be the reason for its low degree of crystallinity and very low proportion and quantum size.

The PXRD patterns of Ni single-atom-supported UiO-66 show that the crystalline structure of as-prepared UiO-66 did not change after metalation of the nickel atoms with their

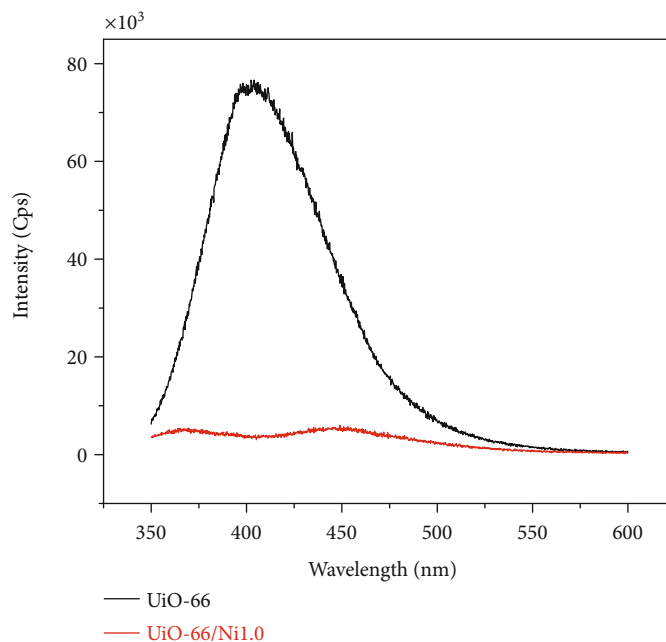


FIGURE 7: Fluorescence spectra of the UiO-66 and UiO-66/Ni1.0.

framework, demonstrating that the chemical structure of the as-prepared UiO-66 with the presence of nickel atoms cannot be destroyed. However, it is difficult to obtain the structure of the Ni single-atom site using the single X-ray diffraction patterns. Thus, in order to investigate the existence of a nickel single atom in the as-prepared UiO-66 structure, the EDX analysis of the as-prepared UiO-66 and UiO-66/Ni x ($x = 0.3, 0.5, 0.7$, and 1.0) samples was performed and is shown in Table 1 and Figures 2(a) and 2(b). These results show that the incorporation of Ni atoms in the UiO-66 structure can be controlled by the amount of NiCl $_2$ ·6H $_2$ O used in the synthesis. The Ni:Zr atomic ratio increased with the increase in the amount of the NiCl $_2$ ·6H $_2$ O precursor from 0.3 to 0.5 mmol and remained constant from 0.7 to 1.0 mmol, demonstrating that the number of defect sites is limited in the as-synthesized UiO-66 structure.

TG-DTA analysis of UiO-66 and UiO-66/Ni1.0 catalysts was also performed to investigate the amount of the missing-linker defects in the UiO-66 structure. As can be seen in Figure 2(c), 31.49% weight loss in the range of 100 to 150°C corresponded to DMF, CH $_3$ OH, and H $_2$ O solvent within the pores of the UiO-66 structure. The second step weight loss of 39.68% after 300°C was attributed to the coordinated ligand with Zr $^{4+}$ cation to form the UiO-66 structure such as H $_2$ BDC and missing-linker defects (-OH/OH $_2$). The final thermal decomposition product of UiO-66 began at 610°C, corresponding to ZrO $_2$. The actual stoichiometric formula weight of as-prepared UiO-66 was calculated by varying the value of x . It was found that the value x of 1 was closely consistent with the calculated weight loss of 39.78%, corresponding that each Zr $_6$ O $_4$ (OH) $_4$ is coordinated to 1 molecule of H $_2$ BDC, 10 molecules of DMF, and 1 molecule of the OH $^-$ group. Hence, the stoichiometric formulae of the as-prepared

UiO-66 can be described as follows: Zr $_6$ O $_4$ (OH) $_4$ (C $_8$ H $_4$ O $_4$)(DMF) $_{10}$ (OH) $_{10}$.

Figure 2(d) illustrates the TG-DTA analysis of the nickel single-atom-incorporated UiO-66 structure (UiO-66/Ni1.0). Similarly, 7.34% of weight loss at 104°C was due to solvent molecules within the pores of the UiO-66/Ni1.0 structure. Then, the composition process of UiO-66/Ni1.0 samples experiences two steps of weight loss of 38.46% prior to the formation of the final ZrO $_2$ and NiO products. It is worth noting that the molar ratio of Ni:Cl of about 1 was calculated by energy-dispersive X-ray spectroscopic (EDX) analysis of these samples of UiO-66/Ni, indicating that Cl $^-$ anion can be seen as a ligand coordinating to Ni $^{2+}$ cation. The stoichiometric formula of the UiO-66/Ni1.0 was also hypothesized as follows: Zr $_6$ O $_4$ (OH) $_4$ (C $_8$ H $_4$ O $_4$)(DMF) $_{10}$ (OH) $_{10-2x}$ Ni $_x$ OH $_x$ (Cl) $_x$. The result suggested that the value x of 2 was closely consistent with the TG calculated value (49.31%). Hence, the stoichiometric formula of the UiO-66 after metalation with nickel single atoms can be described as follows: Zr $_6$ O $_4$ (OH) $_4$ (C $_8$ H $_4$ O $_4$)(DMF) $_{10}$ (OH) $_8$ Ni $_2$ (OH) $_2$ (Cl) $_2$. This result shows that the ratio of Zr $_6$ /Ni was closely consistent with elemental composition of the as-prepared UiO-66/Ni sample which was determined by EDX analysis.

Figure 3 illustrates the FTIR spectra of as-prepared UiO-66 and the samples of UiO-66/Ni x ($x = 0.3, 0.5, 0.7$, and 1.0). The peaks in the regions of 1650 and 1577 cm $^{-1}$ are attributed to the symmetric stretching vibrations of the carboxylate group which are coordinated with a zirconium center during the deprotonation. Specifically, the peak of the band at 1400 cm $^{-1}$ is associated with C-O root in C-OH of carboxylic acid. The presence of the band at 746 and 659 cm $^{-1}$ corresponded to the stretch vibration of Zr-O clusters and O-H of defect sites where Ni atoms are coordinating to -OH/OH $_2$

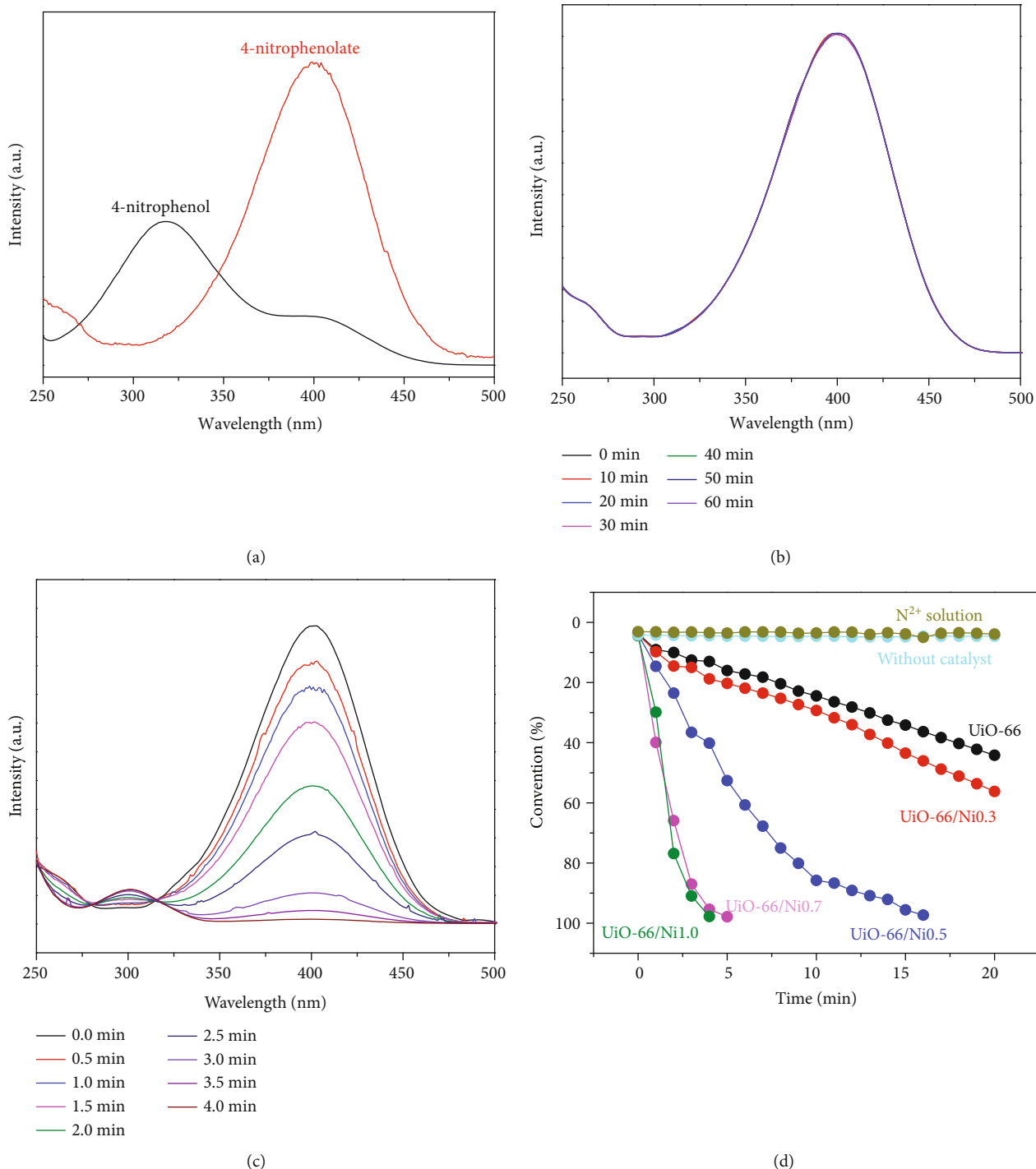


FIGURE 8: UV-vis spectra of 4-NP solution before and after adding NaBH₄ (a); the time-dependent successive reduction of 4-NP with NaBH₄ without catalyst (b); reduction of 4-NP in the presence of UiO-66/Ni1.0 (c); 4-NP conversion (%) of different catalysts (d).

species on UiO-66. The small peaks at 540 and 480 cm⁻¹ can be attributed to the symmetric and asymmetric stretching vibrations of Zr-(OC). It can be clearly observed that the positions of each peak in all samples are well matched together, demonstrating that the incorporation of Ni single atoms does not change the chemical structure of UiO-66 and Ni single atoms that are coordinated to -OH/OH₂ species on defect-free UiO-66 structure.

The morphology of as-prepared UiO-66 and UiO-66/Ni1.0 was clearly observed by using SEM images, as shown in Figures 4(a) and 4(b). The SEM images represented that the as-prepared UiO-66 before and after the incorporation of Ni single atoms were sphere-like particles with uniform size and smooth surface.

In order to further investigate the morphology of the samples and the existence of impurity nanoparticles on the

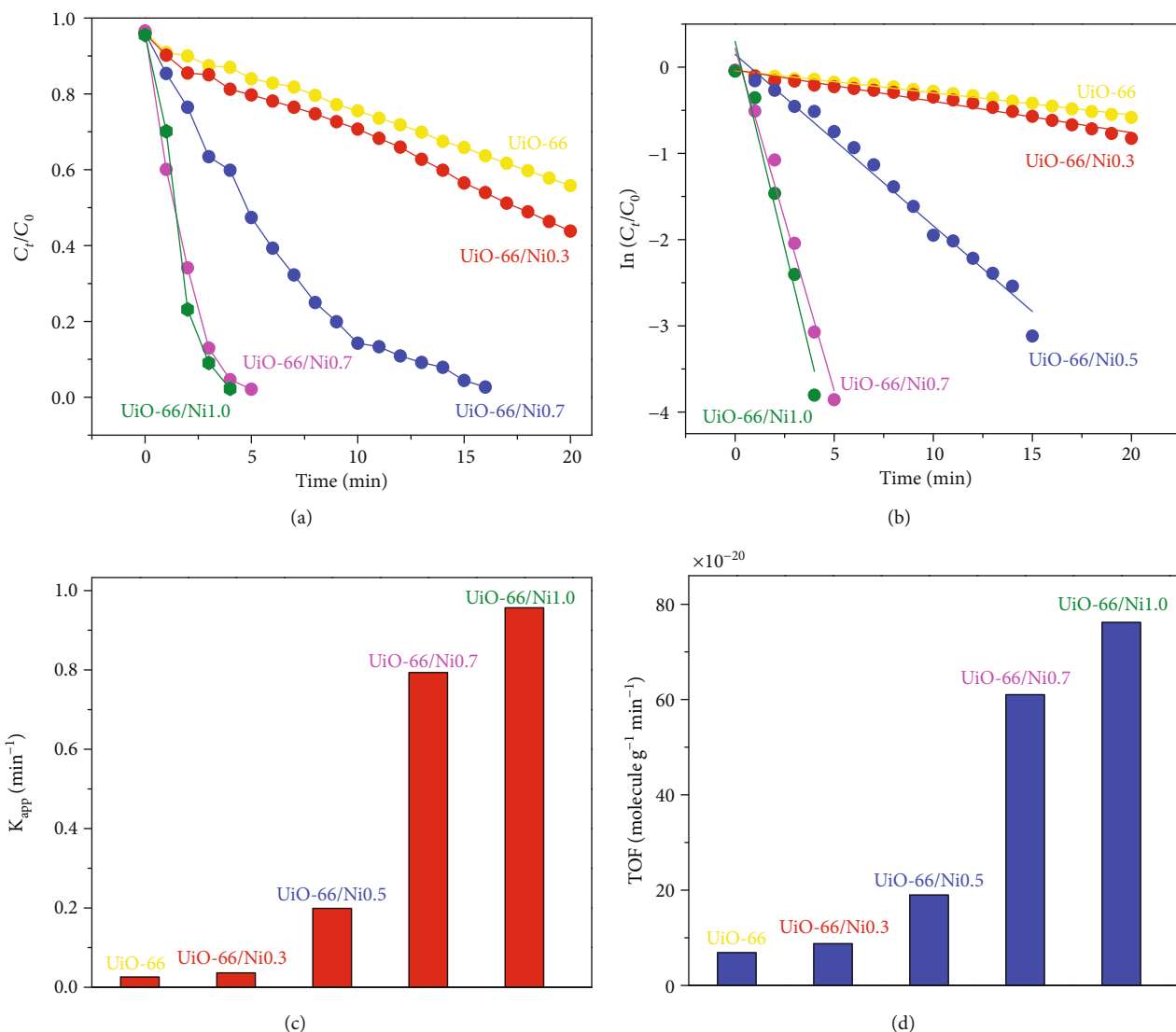


FIGURE 9: Plots of C_t/C_0 (a) and $\ln C_t/C_0$ (b) vs. reaction time and the k_{app} (c) and TOF values (d) of different catalysts.

UiO-66 surface, the TEM images were observed and are exhibited in Figures 4(c) and 4(d). It can be clearly seen that the Ni or NiO nanoparticle formation did not occur on the surface of the UiO-66 structure, which is consistent with the results of XRD patterns of both UiO-66 and UiO-66/Ni1.0.

The nitrogen adsorption-desorption isotherms of the samples of defect-free UiO-66 and UiO-66/Ni1.0 are illustrated in Figure 5. Two isotherms of UiO-66 and UiO-66/Ni1.0 have the similar shape, exhibited typical type I with a H4 hysteresis loop, and possessed mesoporous structure [50].

The pore size distributions and the BET-specific surface area for the samples were obtained by using desorption data by the BJH method. The pore sizes for the samples do not change considerably, about 4.4 and 4.8 nm, respectively.

The specific surface area of as-prepared UiO-66 was 855.06 m² g⁻¹. After metalation with Ni single atoms, the S_{BET} of UiO-66/Ni1.0 catalysts is slightly decreased, about

10 m² g⁻¹ compared to that of as-synthesized UiO-66. These results evidenced that the as-prepared UiO-66 structure is unchangeable after metalation with the Ni single atoms.

The chemical composition and the chemical state of the elements in the sample UiO66/Ni1.0 were determined by using XPS spectra and are presented in Figure 6. As the extensive scan data in Figure 6(a), all the peaks corresponding to the Zr, Ni, O, and C elements have been detected. In addition, the high-resolution spectrum of the sample shows two peaks at 182.74 and 185.03 eV, which could be attributed to Zr 3d_{5/2} and Zr 3d_{3/2} of zirconium in the Zr₆O₄(OH)₄ metal center (Figure 6(b)). The binding energy of Ni 2p_{3/2} and Ni 2p_{1/2} was 855.28 eV and 872.48 eV, respectively. The energy binding distance of Ni 2p_{3/2} and Ni 2p_{1/2} peaks was around 17 eV, indicating that Ni2p belongs to the Ni(II) oxidation state in the UiO-66/Ni structure [51]. Those results demonstrated that Ni single-atom metalation with the UiO-66 structure was successfully synthesized via chemical bonding.

TABLE 2: k_{app} and TOF values for the reduction of 4-NP with different catalysts (the concentration of the catalyst was 8.33 mg L^{-1}).

No.	Samples	TOF ^a $\times 10^{-20}$ (molecule $\text{g}^{-1} \text{min}^{-1}$)	k_{app} (min^{-1})	R^2
1	UiO-66	6.89	0.026	0.991
2	UiO-66/Ni0.3	8.76	0.036	0.975
3	UiO-66/Ni0.5	18.96	0.198	0.985
4	UiO-66/Ni0.7	61.03	0.794	0.983
5	UiO-66/Ni1.0	76.19	0.956	0.964

^aTurnover frequency (TOF) = (molecule of reacted organic substrate/mass of catalyst) \times reaction time (min^{-1}).

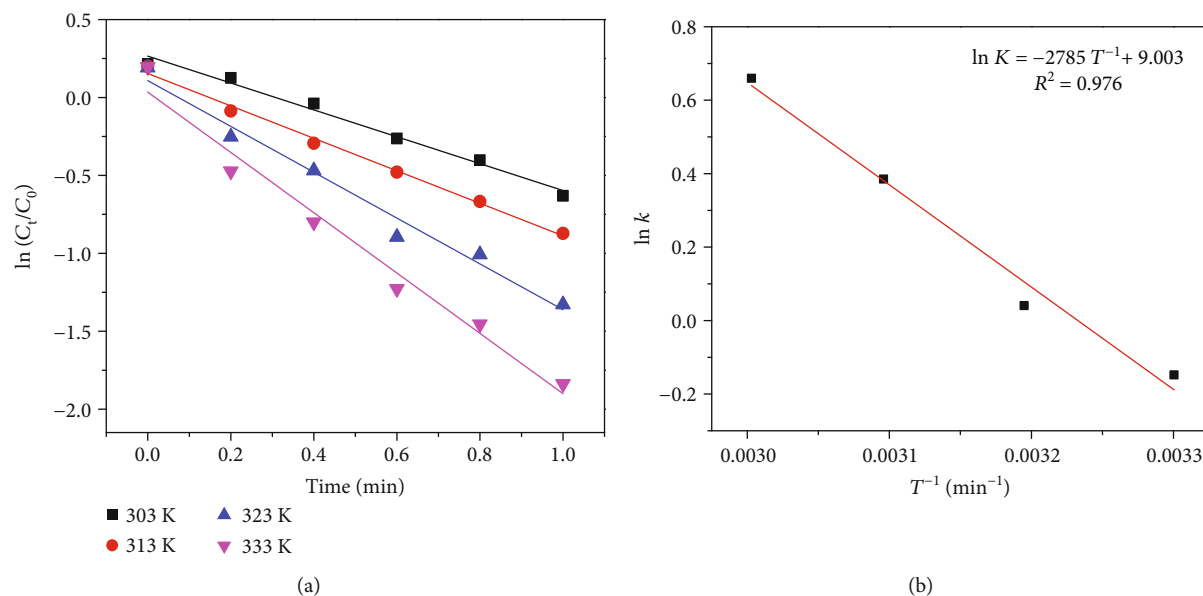


FIGURE 10: Plot of $\ln(C_t/C_0)$ vs. time (a). Arrhenius plot of $\ln K$ vs. $1/T$ for the catalytic reduction of 4-NP using the UiO-66/Ni1.0 catalyst at different temperatures (b).

In order to evaluate the transfer of photogenerated electrons, the photoluminescence quenching of UiO-66 and Ni-supported UiO-66 (UiO-66/Ni1.0) was carried out and is shown in Figure 7. The maximum emission wavelength was observed at 402 nm for UiO-66 when the excitation wavelength was 300 nm. For UiO-66 with the presence of Ni atoms, the fluorescence was completely quenched, indicating that the existence of Ni in the UiO-66 structure plays a vital role in retarding recombination of photoinduced hole-electron pairs.

3.2. Reduction of 4-Nitrophenol Using UiO-66/Ni as a Catalyst

3.2.1. Catalytic Reduction of 4-Nitrophenol. The reduction reaction of 4-nitrophenol with the presence of NaBH_4 solution was used to investigate the catalytic activity of the UiO-66/Ni catalyst.

The catalytic performance of single-atom Ni-supported UiO-66 was investigated using the model of reduction reaction of 4-nitrophenol (4-NP) to 4-aminophenol (4-AP) by NaBH_4 solution. It is clear that the maximum adsorption peak of 4-NP was observed at 317 nm and shifted to 400 nm with the presence of NaBH_4 solution (Figure 8(a)).

TABLE 3: Thermodynamic parameters of the catalytic reduction of 4-NP at different temperatures.

T (K)	k_{app} (min^{-1})	R^2	E_a (kJ mol^{-1})
303	0.862	0.987	23.15
313	1.042	0.994	
323	1.470	0.979	
333	1.934	0.977	

This can be explained by an increase in alkalinity upon addition of NaBH_4 , leading to the formation of 4-nitrophenolate ions which corresponds to a color change from light yellow to deep yellow. As can be seen in Figure 8(b), the maximum adsorption peak at 400 nm remained steady over 60 min after the addition of NaBH_4 , demonstrating that the reduction reaction of 4-NP did not occur with the absence of the catalyst. After the addition of $5 \mu\text{L}$ of the UiO-66/Ni1.0 dispersion liquid, the intensity of characteristic adsorption peak at 400 nm decreased significantly over the reaction process, while the novel maximum adsorption peak was observed at 300 nm and the deep yellow of solution mixture was changed

TABLE 4: Comparison of the activity of various catalysts for the reduction performance toward 4-nitrophenol.

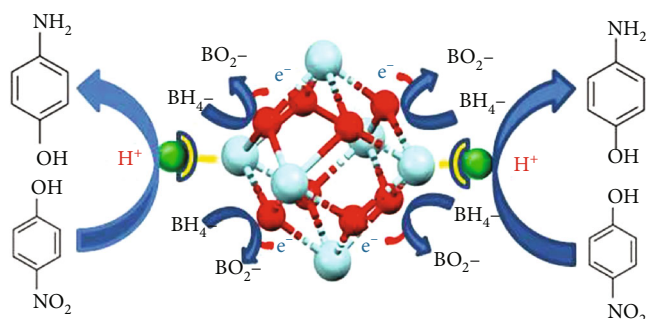
Catalyst	Type	$C_{4\text{-NP}}$ (mM)	C_{catalyst} (mg mL ⁻¹)	Time (min)	K_{app} (min ⁻¹)	Ref
Au@[Na]-HAMS	Yolk-shell mesoporous	5.217	1.739	15	0.310	[59]
Pd/C	Nanoparticles	1.67	0.0024 mM	8	0.529	[60]
Co-Ni double hydroxide	2D graphene-like	0.129	0.323	6	0.669	[61]
Co@C	Porous prisms	0.1	0.02	4	0.660	[62]
Pt/Co ₃ O ₄ -CeO ₂	Mesoporous	0.0958	0.0479	4	0.678	[63]
Ca/Co ₃ O ₄	Mesopore	3.5×10^{-3}	0.08	41.67	0.230	[64]
MoS ₂ /SnO ₂	Hierarchical heterojunction	0.1	0.5	13	0.252	[65]
Pt@Ag	Core-shell nanoparticles	0.1	0.016	8	0.355	[66]

into colorless solution within 4 min, corresponding to the formation of the product of 4-AP (Figure 8(c)).

Figure 8(d) shows the convention of reduction reactions toward 4-NP at different times without a catalyst and the presence of the as-prepared UiO-66 and UiO-66/Nix ($x = 0.3, 0.5, 0.7,$ and 1.0) catalyst, respectively. The 4-NP convention with the presence of NaBH₄ without a catalyst or 0.01 M Ni²⁺ remained stable over 20 min, approximately 5% indicating that NaBH₄ without UiO-66/Ni or NaBH₄ with Ni²⁺ could not reduce 4-NP. This result means that UiO-66/Ni plays an important role as a heterogeneous catalyst for 4-NP reduction. However, in the presence of the as-prepared UiO-66 catalyst, the reduction of 4-NP into the corresponding 4-AP took 20 min for the conversion of 44%; this figure was 56% for UiO-66/Ni0.3. It is noticeable that it took around 9 min for UiO-66/Ni0.5 for 99% conversion, while the UiO-66/Ni0.7 and UiO-66/Ni1.0 catalysts needed only 3 min and 4 min, respectively, to complete the reduction of 4-NP. The results demonstrated that the presence of nickel single-atom-supported UiO-66 structure plays a crucial role in the excellent catalytic performance toward 4-NP reduction. Specifically, the optimal amount of the NiCl₂·6H₂O precursor, introduced in the UiO-66 structure, was 1.0 mmol (UiO-66/Ni1.0 catalyst) indicating the best catalytic performance.

Figure 9(a) illustrates the plot of C_t/C_0 versus reaction time of each catalyst, where C_t and C_0 represent the concentration of 4-NP at the time of t and 0 min, respectively. The catalytic performance of all as-prepared samples was monitored by UV-vis spectrometry at the interval time of 1 min. The plots of $\ln(C_t/C_0)$ versus reaction time for the reduction of 4-NP are shown in Figure 9(b). The excess of concentration of NaBH₄ can be considered a constant during the reaction progress. Thus, the pseudo-first-order kinetics was employed to investigate the reduction reaction of 4-NP. The linear fit with a coefficient of determination very close to unity also supports the assumption of the pseudo-first-order kinetics. The apparent rate constant values (k_{app}) were found to be 0.026, 0.036, 0.198, 0.794, and 0.95 min⁻¹ for the UiO-66, UiO-66/Ni0.3, UiO-66/Ni0.5, UiO-66/Ni0.7, and UiO-66/Ni1.0 catalysts, respectively, using the following equation:

$$-\frac{dC_t}{dt} = k_{\text{app}} C_t, \quad (2)$$



SCHEME 2: Proposed mechanism for the reduction of 4-nitrophenol using the UiO-66/Ni1.0 catalyst.

where C_t was the concentration of 4-NP at time t and k_{app} was the apparent rate constant.

The detailed results are represented in Table 1 and Figure 9(c). The apparent rate constant values (k_{app}) increase significantly with an increase in the amount of Ni in the UiO-66 structure. The UiO-66/Ni1.0 catalyst showed the highest k_{app} compared to as-prepared UiO-66 and different UiO-66/Nix ($x = 0.3, 0.5,$ and 0.7). The TOF values were calculated, and the results are shown in Figure 9(d) and Table 2. The catalytic reduction reaction toward 4-nitrophenol was also evaluated by using the TOF values. As can be seen in Figure 9(d) and Table 2, the TOF values were calculated to be 6.89×10^{20} , 8.76×10^{20} , 18.96×10^{20} , 61.03×10^{20} , and 76.19×10^{20} molecules g⁻¹ min⁻¹ for UiO-66, UiO-66/Ni0.3, UiO-66/Ni0.5, UiO-66/Ni0.7, and UiO-66/Ni1.0, respectively. The increase in the TOF value can be attributed to the increased amount of active nickel catalyst sites which are present in UiO-66 network and the facile diffusion routes of the reactant molecules to the active sites in porous structure.

In order to determine the apparent activation energy (E_a) of the reduction reaction of 4-NP using UiO-66/Ni1.0 as the catalyst, the reaction kinetics was conducted over the temperature range of 303–343 K (Figure 10). The extraction of the apparent activation energy E_a from the Arrhenius equation (3) is determined to be 23.15 kJ mol⁻¹ for the UiO-66/Ni1.0 catalyst (Table 3).

$$\ln k_{\text{app}} = \ln A - \frac{E_a}{RT}. \quad (3)$$

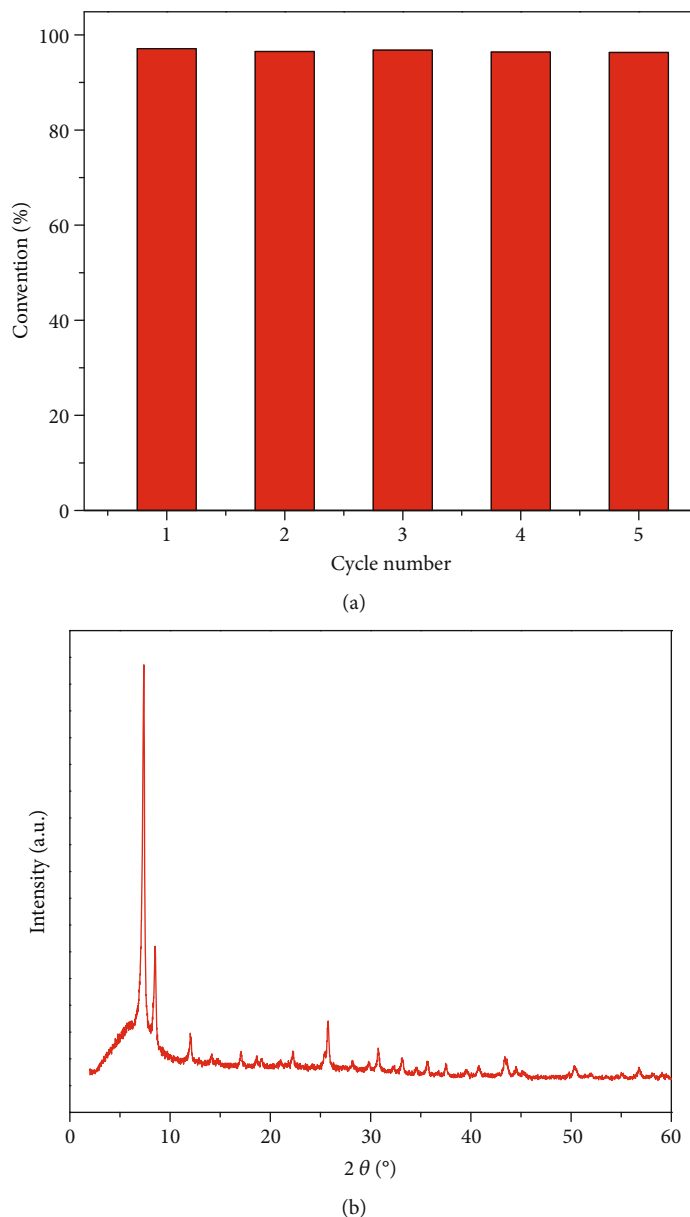


FIGURE 11: Recyclability of the 4-nitrophenol reduction reaction using the UiO-66/Ni1.0 catalyst (a) and XRD patterns of the 5th reused UiO-66/Ni1.0 catalyst (b).

The obtained results show that the UiO-66/Ni1.0 catalyst can significantly decrease the activation energy and increase the apparent rate constants of 4-NP catalytic reduction.

The comparison of the various catalysts in previously published papers for the reduction performance toward 4-nitrophenol is listed in Table 4. It is clear that the UiO-66/Ni1.0 catalyst exhibits the highest catalytic activity for 4-NP reduction. For example, k_{app} is 0.529 min^{-1} for Pd/C NPs, 0.660 min^{-1} for porous prisms Co@C NPs, and 0.335 min^{-1} for core-shell nanoparticles Pt@Ag, which are lower than 0.956 of UiO-66/Ni1.0.

3.2.2. The Mechanism of the 4-Nitrophenol Reduction Reaction Using the UiO-66/Ni1.0 Catalyst. The excellent catalytic performance of the UiO-66/Ni1.0 can be ascribed

to the high activity of the nickel single-atom-supported UiO-66 network and the excellent permeability of the porous structure. In this study, the mechanism of the 4-nitrophenol reduction reaction can be described in Scheme 2.

Initially, the 4-nitrophenol can easily penetrate and diffuse into the inner pore spaces of the UiO-66/Ni1.0 catalytic structure. Then, 4-nitrophenol molecules were rapidly absorbed on the Ni(II) active sites which are present in the UiO-66 structure, thanks to the high electrical transport of the Ni(II) active sites, which can facilitate the electron transfer from BH_4^- to 4-NP and reduce the activation energy. At last, 4-AP can be formed efficiently through the hydrogenation reduction of 4-NP and diffused conveniently from the nanoporous structure via the abundant mesopores.

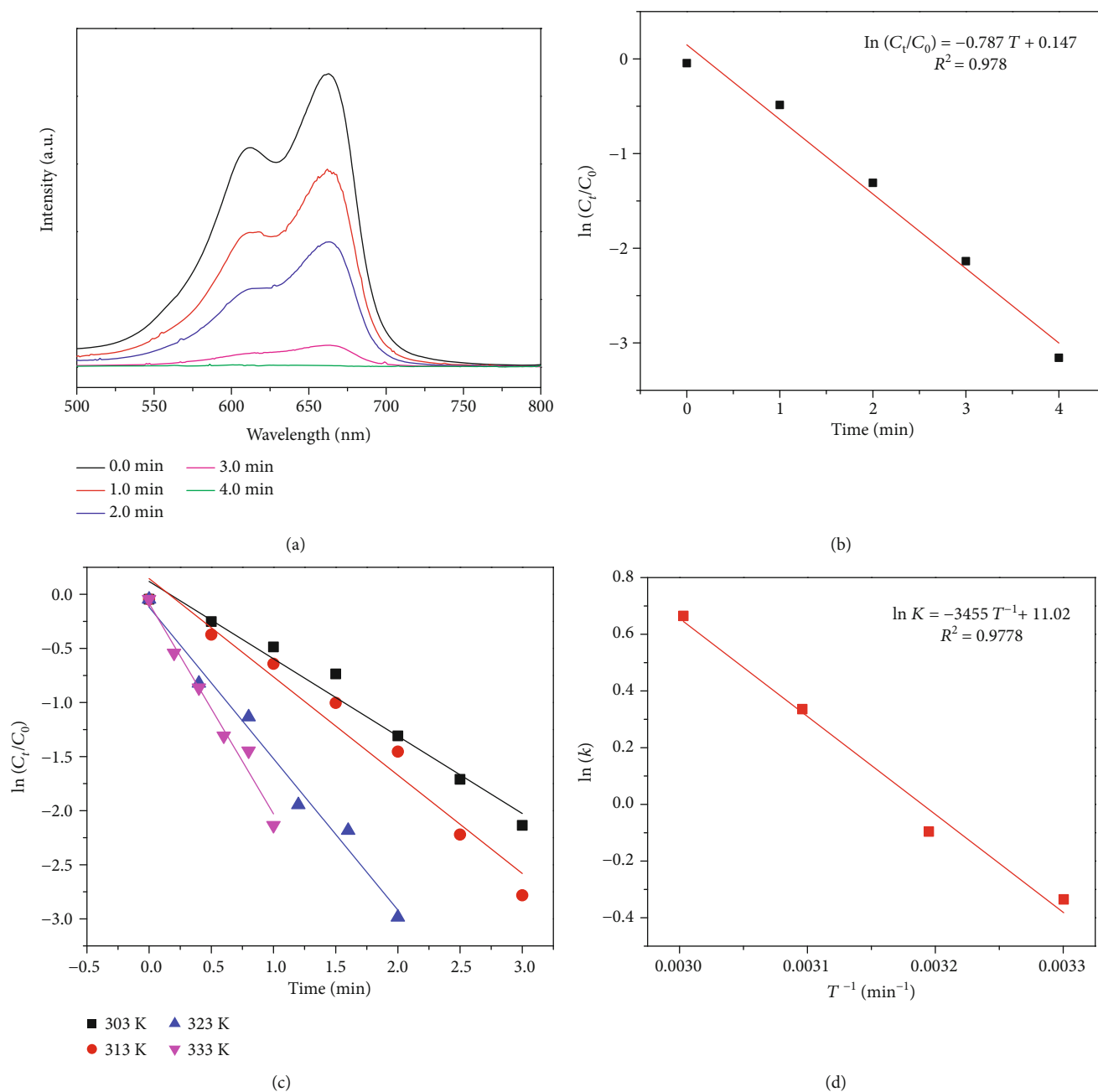


FIGURE 12: UV-vis absorption spectrum changes in MB solution catalyzed by UiO-66/Ni1.0 (a); plot of $\ln(C_t/C_0)$ vs. time corresponding to (a) (b); plot of $\ln(C_t/C_0)$ vs. time (c); Arrhenius plot (a) of $\ln k$ vs. $1/T$ for the catalytic reduction of MB in the presence of UiO-66/Ni1.0 at different temperatures (d).

3.2.3. Recyclability of the UiO-66/Ni1.0 Catalyst. The recyclability of the catalyst plays an important role in the heterogeneous catalytic reaction. In order to evaluate the recyclability of the catalyst, 5 cycles of 4-nitrophenol catalytic reduction were performed with the UiO-66/Ni1.0 catalyst. As can be seen in Figure 11(a), during the 5 cycles, the conversion of 4-nitrophenol was more than 95% within 4 min of the reaction process. The XRD pattern of the 5th reused UiO-66/Ni1.0 catalyst is shown in Figure 11(b). The intensity of the characteristic peak after the 5th recycle indicates that the UiO-66/Ni1.0 preserved the high degree of crystallinity

of the UiO-66 framework. The results show that the UiO-66/Ni1.0 catalyst possesses the excellent stability and recyclability of the UiO-66/Ni.

3.3. Catalytic Performance of UiO-66/Ni1.0 for MB. To further evaluate the catalytic performance of UiO-66/Ni1.0, the catalytic reduction of MB in the presence of NaBH_4 as the reduction agent was also investigated and is shown in Figure 12 and Table 5.

In the presence of $5\mu\text{L}$ of the obtained UiO-66/Ni dispersion liquid (5 mg mL^{-1}), the color of MB solution with the

TABLE 5: Thermodynamic parameters of the catalytic reduction of MB at different temperatures.

T (K)	k_{app} (min^{-1})	R^2	E_a (kJ mol^{-1})
303	0.715	0.973	28.72
313	0.909	0.967	
323	1.399	0.983	
333	1.944	0.978	

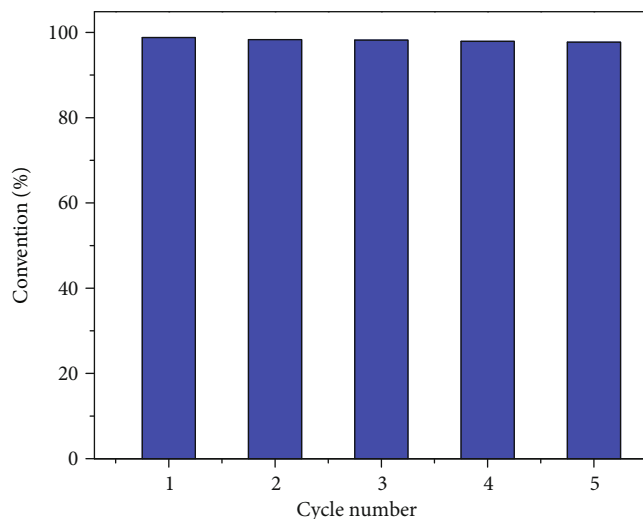


FIGURE 13: Recyclability of the MB reduction reaction using the UiO-66/Ni1.0 catalyst.

intensity of the characteristic adsorption peak at 664 nm disappeared swiftly within 4 min (Figure 12(a)). The MB decolorization kinetics followed the pseudo-first-order kinetics model (Figure 12(b)). Moreover, the k_{app} and TOF for the reduction of MB using UiO-66/Ni1.0 at room temperature are 0.787min^{-1} and 33.89×10^{20} molecules $\text{g}^{-1} \text{min}^{-1}$, respectively. The apparent activation energy E_a is determined to be $28.72 \text{ kJ mol}^{-1}$ (Table 5 and Figure 12(d)). The apparent kinetic rate constant for MB decolorization is found to be several ten to hundred times greater than those for photocatalysts in previous publications [52–54] and is much higher than that for MB decolorization with NaBH_4 as a reduction agent on the CuNPs@Gelatin catalyst [55], $\text{Fe}_3\text{O}_4/\text{SiO}_2/\text{Au}/\text{por-SiO}_2$ catalyst [56], Ag/PSNM nanocomposite spheres [57], and Ag, Au nanoparticles [58]. These results show that UiO-66/Ni exhibits excellent catalytic performance for the hydrogenation of MB.

Similarly, the recyclability of the synthesized catalyst for the purpose of MB degradation was also assessed. The MB reduction reaction was repeated for five cycles, and the conversion remained almost constant, more than 97% within 4 min, as can be seen in Figure 13.

4. Conclusion

In this research, a novel single-atom Ni heterogeneous catalyst-supported UiO-66 structure has been successfully

synthesized through a postsynthetic metalation method. This structure possesses the well-defined active site with a high specific surface area, where single Ni atoms are anchored to the oxygen atoms of $-\text{OH}/\text{OH}_2$ capping the defect sites on the Zr oxide clusters of UiO-66. The as-synthesized catalyst was employed to investigate the reduction reaction of 4-nitrophenol or methylene blue with the presence of NaBH_4 . It was found that this catalyst exhibits excellent catalytic activity and high stability. It is expected that this research would pave the way for the construction of other single-site heterogeneous catalysts for wide applications.

Data Availability

The data used to support the findings of this study are available from the corresponding author upon request.

Conflicts of Interest

The authors declare that they have no conflicts of interest.

Acknowledgments

This work was supported by Hue University under Decision DHH 2020-01-170.

References

- [1] P. K. Arora, A. Srivastava, and V. P. Singh, “Bacterial degradation of nitrophenols and their derivatives,” *Journal of Hazardous Materials*, vol. 266, pp. 42–59, 2014.
- [2] Y. Li, W. P. Hsieh, R. Mahmudov, X. Wei, and C. P. Huang, “Combined ultrasound and Fenton (US-Fenton) process for the treatment of ammunition wastewater,” *Journal of Hazardous Materials*, vol. 244–245, pp. 403–411, 2013.
- [3] Z. Fang, J. Chen, X. Qiu, X. Qiu, W. Cheng, and L. Zhu, “Effective removal of antibiotic metronidazole from water by nanoscale zero-valent iron particles,” *Desalination*, vol. 268, no. 1–3, pp. 60–67, 2011.
- [4] Y. Yuan, B. Lai, and Y. Y. Tang, “Combined Fe^0/air and Fenton process for the treatment of dinitrophenol (DDNP) industry wastewater,” *Chemical Engineering Journal*, vol. 283, pp. 1514–1521, 2016.
- [5] B. Petrova, B. Tsyntsarski, T. Budinova, N. Petrov, L. F. Velasco, and C. O. Ania, “Activated carbon from coal tar pitch and furfural for the removal of p-nitrophenol and m-aminophenol,” *Chemical Engineering Journal*, vol. 172, no. 1, pp. 102–108, 2011.
- [6] Z. Xiong, B. Lai, Y. Yuan, J. Cao, P. Yang, and Y. Zhou, “Degradation of p-nitrophenol (PNP) in aqueous solution by a micro-size Fe^0/O_3 process (mFe^0/O_3): Optimization, kinetic, performance and mechanism,” *Chemical Engineering Journal*, vol. 302, pp. 137–145, 2016.
- [7] S. Chiron, L. Comoretto, E. Rinaldi, V. Maurino, C. Minero, and D. Vione, “Pesticide by-products in the Rhone delta (Southern France). The case of 4-chloro-2-methylphenol and of its nitroderivative,” *Chemosphere*, vol. 74, no. 4, pp. 599–604, 2009.
- [8] Z. I. Bhatti, H. Toda, and K. Furukawa, “p-Nitrophenol degradation by activated sludge attached on nonwovens,” *Water Research*, vol. 36, no. 5, pp. 1135–1142, 2002.

- [9] C. Qiu, X. Li, H. Wang et al., "Investigation of the synergistic effects for *p*-nitrophenol mineralization by a combined process of ozonation and electrolysis using a boron-doped diamond anode," *Journal of Hazardous Materials*, vol. 280, pp. 644–653, 2014.
- [10] B. Lai, Y. H. Zhang, R. Li, Y. X. Zhou, and J. Wang, "Influence of operating temperature on the reduction of high concentration *p*-nitrophenol (PNP) by zero valent iron (ZVI)," *Chemical Engineering Journal*, vol. 249, pp. 143–152, 2014.
- [11] G. Eichenbaum, D. Kirkland, P. O'Neill et al., "Assessment of the genotoxic and carcinogenic risks of *p*-nitrophenol when it is present as an impurity in a drug product," *Regulatory Toxicology and Pharmacology*, vol. 55, no. 1, pp. 33–42, 2009.
- [12] E. Fernandes Silva, A. S. Varela Junior, T. F. Cardoso et al., "Reproductive toxicology of 2,4 dinitrophenol in boar sperm," *Toxicology in Vitro*, vol. 35, pp. 31–35, 2016.
- [13] J. Chen, M. Song, Y. Li, Y. Zhang, K. Taya, and C. M. Li, "The effect of phytosterol protects rats against 4-nitrophenol-induced liver damage," *Environmental Toxicology and Pharmacology*, vol. 41, pp. 266–271, 2016.
- [14] E. Forgacs, T. Cserhati, and G. Oros, "Removal of synthetic dyes from wastewaters: a review," *Environment International*, vol. 30, no. 7, pp. 953–971, 2004.
- [15] B. K. Ghosh, S. Hazra, B. Naik, and N. N. Ghosh, "Preparation of Cu nanoparticle loaded SBA-15 and their excellent catalytic activity in reduction of variety of dyes," *Powder Technology*, vol. 269, pp. 371–378, 2015.
- [16] J. K. Ahmed and M. Ahmaruzzaman, "A facile synthesis of Fe₃O₄-charcoal composite for the sorption of a hazardous dye from aquatic environment," *Journal of Environmental Management*, vol. 163, pp. 163–173, 2015.
- [17] I. Ali, "New generation adsorbents for water treatment," *Chemical Reviews*, vol. 112, no. 10, pp. 5073–5091, 2012.
- [18] J. N. Tiwari, N. H. le, K. C. Kemp et al., "Reduced graphene oxide-based hydrogels for the efficient capture of dye pollutants from aqueous solutions," *Carbon*, vol. 56, pp. 173–182, 2013.
- [19] T. Zhu, J. S. Chen, and X. W. D. Lou, "Highly efficient removal of organic dyes from waste water using hierarchical NiO spheres with high surface area," *Journal of Physical Chemistry C*, vol. 116, no. 12, pp. 6873–6878, 2012.
- [20] M. Panizza and G. Cerisola, "Direct and mediated anodic oxidation of organic pollutants," *Chemical Reviews*, vol. 109, no. 12, pp. 6541–6569, 2009.
- [21] O. A. Zeleke and D. H. Kuo, "Synthesis of a hierarchical structured NiO/NiS composite catalyst for reduction of 4-nitrophenol and organic dyes," *RSC Advances*, vol. 7, no. 8, pp. 4353–4362, 2017.
- [22] R. J. Tayade, T. S. Natarajan, and H. C. Bajaj, "Photocatalytic degradation of methylene blue dye using ultraviolet light emitting diodes," *Industrial & Engineering Chemistry Research*, vol. 48, no. 23, pp. 10262–10267, 2009.
- [23] J. A. Laszlo, "Regeneration of dye-saturated quaternized cellulose by bisulfite-mediated borohydride reduction of dye azo groups: an improved process for decolorization of textile wastewaters," *Environmental Science & Technology*, vol. 31, no. 12, pp. 3647–3653, 1997.
- [24] J. Liu, J. Yang, H. Ma et al., "Facile synthesis of carbon-doped mesoporous anatase TiO₂ for the enhanced visible-light driven photocatalysis," *Chemical Communications*, vol. 50, no. 90, pp. 13971–13974, 2014.
- [25] Z. Li and Q. Xu, "Metal-nanoparticle-catalyzed hydrogen generation from formic acid," *Accounts of Chemical Research*, vol. 50, no. 6, pp. 1449–1458, 2017.
- [26] Q. Yang, Q. Xu, and H. L. Jiang, "Metal-organic frameworks meet metal nanoparticles: synergistic effect for enhanced catalysis," *Chemical Society Reviews*, vol. 46, no. 15, pp. 4774–4808, 2017.
- [27] R. H. Crabtree, "Deactivation in homogeneous transition metal catalysis: causes, avoidance, and cure," *Chemical reviews*, vol. 115, no. 1, pp. 127–150, 2015.
- [28] Q. Wang and D. Astruc, "State of the art and prospects in metal-organic framework (MOF)-based and MOF-derived nanocatalysis," *Chemical Reviews*, vol. 120, no. 2, pp. 1438–1511, 2020.
- [29] L. Liu and A. Corma, "Metal catalysts for heterogeneous catalysis: from single atoms to nanoclusters and nanoparticles," *Chemical Reviews*, vol. 118, no. 10, pp. 4981–5079, 2018.
- [30] Z. Liang, C. Qu, D. Xia, R. Zou, and Q. Xu, "Atomically dispersed metal sites in MOF-based materials for electrocatalytic and photocatalytic energy conversion," *Angewandte Chemie International Edition*, vol. 57, no. 31, pp. 9604–9633, 2018.
- [31] L. Jiao and H. L. Jiang, "Metal-organic-framework-based single-atom catalysts for energy applications," *Chem*, vol. 5, no. 4, pp. 786–804, 2019.
- [32] Y. Wang, J. Mao, X. Meng, L. Yu, D. Deng, and X. Bao, "Catalysis with two-dimensional materials confining single atoms: concept, design and applications," *Chemical reviews*, vol. 119, no. 3, pp. 1806–1854, 2019.
- [33] B. F. Hoskins and R. Robson, "Design and construction of a new class of scaffolding-like materials comprising infinite polymeric frameworks of 3D-linked molecular rods. a reappraisal of the zinc cyanide and cadmium cyanide structures and the synthesis and structure of the diamond-related frameworks [N(CH₃)₄][CuIZnII(CN)₄] and CuI[4,4',4'',4'''-tetracyanotetraphenylmethane]BF₄·x C₆H₅NO₂," *Journal of the American Chemical Society*, vol. 112, no. 4, pp. 1546–1554, 1990.
- [34] S. KITAGAWA, S. MATSUYAMA, M. MUNAKATA, and T. EMORI, "Synthesis and crystal structures of novel one-dimensional polymers, [M(bpen)X]_∞ [M = Cu^I, X = PF₆⁻; M = Ag^I, X = ClO₄⁻; bpen = *trans*-1,2-bis(2-pyridyl)ethylenel] and [Cu(bpen)(CO)(CH₃CN)PF₆]_∞," *Journal of the Chemical Society, Dalton Transactions*, vol. 11, no. 11, pp. 2869–2874, 1991.
- [35] D. Riou and G. Férey, "Hybrid open frameworks (MIL-*n*). Part 3 crystal structures of the HT and LT forms of MIL-7: a new vanadium propylenediphosphonate with an open-framework. Influence of the synthesis temperature on the oxidation state of vanadium within the same structural type," *Journal of Materials Chemistry*, vol. 8, no. 12, pp. 2733–2735, 1998.
- [36] H. C. Zhou, J. R. Long, and O. M. Yaghi, "Introduction to metal-organic frameworks," *Chemical Reviews*, vol. 112, no. 2, pp. 673–674, 2012.
- [37] O. K. Farha, I. Eryazici, C. D. Malliakas et al., "De novo synthesis of a metal-organic framework material featuring ultrahigh surface area and gas storage capacities," *Nature Chemistry*, vol. 2, no. 11, pp. 944–948, 2010.
- [38] G. Lu and J. T. Hupp, "Metal-organic frameworks as sensors: a ZIF-8 based Fabry-Pérot device as a selective sensor for chemical vapors and gases," *Journal of the American Chemical Society*, vol. 132, no. 23, pp. 7832–7833, 2010.

- [39] J. R. Li, R. J. Kuppler, and H. C. Zhou, "Selective gas adsorption and separation in metal-organic frameworks," *Chemical Society Reviews*, vol. 38, no. 5, pp. 1477–1504, 2009.
- [40] N. C. Thacker, Z. Lin, T. Zhang, J. C. Gilhula, C. W. Abney, and W. Lin, "Robust and porous β -diketiminato-functionalized metal-organic frameworks for earth-abundant-metal-catalyzed C-H amination and hydrogenation," *Journal of the American Chemical Society*, vol. 138, no. 10, pp. 3501–3509, 2016.
- [41] H. Furukawa, Y. B. Zhang, J. Jiang et al., "Water adsorption in porous metal-organic frameworks and related materials," *Journal of the American Chemical Society*, vol. 136, no. 11, pp. 4369–4381, 2014.
- [42] Z. Fang, J. P. Dürholt, M. Kauer et al., "Structural complexity in metal-organic frameworks: simultaneous modification of open metal sites and hierarchical porosity by systematic doping with defective linkers," *Journal of the American Chemical Society*, vol. 136, no. 27, pp. 9627–9636, 2014.
- [43] B. Tu, Q. Pang, D. Wu, Y. Song, L. Weng, and Q. Li, "Ordered vacancies and their chemistry in metal-organic frameworks," *Journal of the American Chemical Society*, vol. 136, no. 41, pp. 14465–14471, 2014.
- [44] Q. Zhao, W. Yuan, J. Liang, and J. Li, "Synthesis and hydrogen storage studies of metal-organic framework UiO-66," *International Journal of Hydrogen Energy*, vol. 38, no. 29, pp. 13104–13109, 2013.
- [45] H. Wu, V. Krungleviciute, M. Tyagi et al., "Unusual and highly tunable missing-linker defects in zirconium metal-organic framework UiO-66 and their important effects on gas adsorption," *Journal of the American Chemical Society*, vol. 135, no. 28, pp. 10525–10532, 2013.
- [46] L. Valenzano, S. Chavan, S. Bordiga et al., "Disclosing the complex structure of UiO-66 metal organic framework: a synergic combination of experiment and theory," *Chemistry of Materials*, vol. 23, no. 7, pp. 1700–1718, 2011.
- [47] S. Øien, H. Reinsch, S. Svelle et al., "Detailed structure analysis of atomic positions and defects in zirconium metal-organic frameworks," *Crystal Growth & Design*, vol. 14, no. 11, pp. 5370–5372, 2014.
- [48] K. Manna, Z. Lin, F. X. Greene et al., "Chemoselective single-site Earth-abundant metal catalysts at metal-organic framework nodes," *Nature Communications*, vol. 7, no. 1, pp. 1–11, 2016.
- [49] S. Kim, J. Lee, S. Jeoung, H. R. Moon, and M. Kim, "Surface-deactivated core-shell metal-organic framework by simple ligand exchange for enhanced size discrimination in aerobic oxidation of alcohols," *Chemistry—A European Journal*, vol. 26, no. 34, pp. 7568–7572, 2020.
- [50] Y. He, "UiO-66-NDC (1,4-naphthalenedicarboxylic acid) as a novel fluorescent probe for the selective detection of Fe^{3+} ," *Journal of Solid State Chemistry*, vol. 285, article 121206, 2020.
- [51] M. C. Biesinger, B. P. Payne, L. W. M. Lau, A. Gerson, and R. S. C. Smart, "X-ray photoelectron spectroscopic chemical state quantification of mixed nickel metal, oxide and hydroxide systems," *Surface and Interface Analysis: An International Journal devoted to the development and application of techniques for the analysis of surfaces, interfaces and thin films*, vol. 41, no. 4, pp. 324–332, 2009.
- [52] A. Houas, H. Lachheb, M. Ksibi, E. Elaloui, C. Guillard, and J. M. Herrmann, "Photocatalytic degradation pathway of methylene blue in water," *Applied Catalysis B: Environmental*, vol. 31, no. 2, pp. 145–157, 2001.
- [53] D. Caschera, T. de Caro, B. Cortese et al., "Fabrication of Eu-TiO₂ NCs functionalized cotton textile as a multifunctional photocatalyst for dye pollutants degradation," *Applied Surface Science*, vol. 427, pp. 81–91, 2018.
- [54] W. Wang, K. Xiao, L. Zhu, Y. Yin, and Z. Wang, "Graphene oxide supported titanium dioxide & ferroferric oxide hybrid, a magnetically separable photocatalyst with enhanced photocatalytic activity for tetracycline hydrochloride degradation," *RSC Advances*, vol. 7, no. 34, pp. 21287–21297, 2017.
- [55] A. Musa, M. B. Ahmad, M. Z. Hussein, M. I. Saiman, and H. A. Sani, "Effect of gelatin-stabilized copper nanoparticles on catalytic reduction of methylene blue," *Nanoscale Research Letters*, vol. 11, no. 1, p. 438, 2016.
- [56] J. Ge, Q. Zhang, T. Zhang, and Y. Yin, "Core-satellite nanocomposite catalysts protected by a porous silica shell: controllable reactivity, high stability, and magnetic recyclability," *Angewandte Chemie*, vol. 47, no. 46, pp. 8924–8928, 2008.
- [57] G. Liao, Q. Li, W. Zhao, Q. Pang, H. Gao, and Z. Xu, "In-situ construction of novel silver nanoparticle decorated polymeric spheres as highly active and stable catalysts for reduction of methylene blue dye," *Applied Catalysis A: General*, vol. 549, pp. 102–111, 2018.
- [58] V. S. Suvith and D. Philip, "Catalytic degradation of methylene blue using biosynthesized gold and silver nanoparticles," *Spectrochimica Acta Part A: Molecular and Biomolecular Spectroscopy*, vol. 118, pp. 526–532, 2014.
- [59] X. Fang, M. F. Hsieh, M. Chen et al., "Hollow mesoporous aluminosilica spheres with perpendicular pore channels as catalytic nanoreactors," *ACS Nano*, vol. 6, no. 5, pp. 4434–4444, 2012.
- [60] F. Paquin, J. Rivnay, A. Salleo, N. Stingelin, and C. Silva-Acuña, "Multi-phase microstructures drive exciton dissociation in neat semicrystalline polymeric semiconductors," *Journal of Materials Chemistry C*, vol. 3, no. 41, pp. 10715–10722, 2015.
- [61] J. M. Song, J. Zhang, D. Ling et al., "A facile synthesis of graphene-like cobalt-nickel double hydroxide nanocomposites at room temperature and their excellent catalytic and adsorption properties," *Journal of Nanoparticle Research*, vol. 16, no. 2, article 2269, 2014.
- [62] H. Li, L. Chi, C. Yang, L. Zhang, F. Yue, and J. Wang, "MOF derived porous Co@C hexagonal-shaped prisms with high catalytic performance," *Journal of Materials Research*, vol. 31, no. 19, pp. 3069–3077, 2016.
- [63] Q. Wang, Y. Zhang, Y. Zhou et al., "Preparation of platinum nanoparticles immobilized on ordered mesoporous Co₃O₄-CeO₂ composites and their enhanced catalytic activity," *RSC Advances*, vol. 6, no. 71, pp. 67173–67183, 2016.
- [64] B. M. Mogudi, P. Ncube, N. Bingwa, N. Mawila, S. Mathebula, and R. Meijboom, "Promotion effects of alkali- and alkaline earth metals on catalytic activity of mesoporous Co₃O₄ for 4-nitrophenol reduction," *Applied Catalysis B: Environmental*, vol. 218, pp. 240–248, 2017.
- [65] X. Q. Qiao, D. F. Hou, D. S. Li et al., "Tunable MoS₂/SnO₂P-N heterojunctions for an efficient trimethylamine gas sensor and 4-nitrophenol reduction catalyst," *ACS Sustainable Chemistry & Engineering*, vol. 6, no. 9, pp. 12375–12384, 2018.
- [66] Z. S. Lv, X. Y. Zhu, H. B. Meng, J. J. Feng, and A. J. Wang, "One-pot synthesis of highly branched core-shell nanoparticles as a recyclable catalyst with dramatically boosting the catalytic performance for 4-nitrophenol reduction," *Journal of Colloid and Interface Science*, vol. 538, pp. 349–356, 2018.